ISTITUTO NAZIONALE DI RICERCA METROLOGICA
Repository Istituzionale

Quantitative three-dimensional characterization of critical sizes of non-spherical TiO2 nanoparticles by using atomic force microscopy

(Article begins on next page)

21 May 2024

Quantitative Three-Dimensional Characterization of Critical Sizes of Non-Spherical TiO₂ Nanoparticles by using Atomic Force Microscopy

Valter Maurino (1,2), Francesco Pellegrino (1,2), Gian Bartolo Picotto (3), Luigi Ribotta* (3,4)

(1) Department of Chemistry and Centro Interdipartimentale NIS, Università degli di Torino, Via Pietro Giuria 7, 10125, Torino, Italy
(2) UniTO-ITT Joint Lab, Via Gioacchino Quarello 15/A, 10135, Torino, Italy
(3) Istituto Nazionale di Ricerca Metrologica (INRiM), Strada delle Cacce 91, 10135, Torino, Italia
(4) Politecnico di Torino, Corso Duca degli Abruzzi 24, Torino, 10129, Italia

*corresponding author: l.ribotta@inrim.it

Highlights

- Complex shapes NP are characterized by AFM
- Geometrical approaches are implemented to determine NP size and AFM tip dilation
- Studied anatase bipyramids and nanosheets may apply as candidate reference materials
- NPs' shape and texture descriptors are investigated to qualify synthetized batches

Abstract

Since both size and shape of nanoparticles are challenging to be quantitatively measured, traceable 3D measurements are nowadays an issue. 3D nanometrology plays a crucial role to reduce the uncertainty of measurements, improve traceable calibration of samples and implement new approaches, models, and methodologies in the study of the nanomaterials.

AFM measurement of nanoparticles with unusual shape represent a non-trivial challenge due to the convolution with the finite size of the tip. In this work, geometric approaches for the determination of critical sizes of TiO₂ anatase bipyramids and nanosheets are described. An uncertainty budget is estimated for each nanoparticle size with the aim of assessing the different sources of error to obtain a more reliable and consistent result. The combined standard uncertainties are respectively less than 5% and 10% of the dimensions of bipyramids and nanosheets. Due to the stability and monomodal distribution of their critical sizes, bipyramids and nanosheets are suitable to apply as candidate reference materials at the nanoscale.

Moreover, quantitative measurements of shape and texture descriptors are discussed in order to understand the quality of the synthetized batch.

Keywords

TiO₂ anatase nanoparticles (NPs), Atomic Force Microscopy (AFM), candidate reference nanomaterials, texture parameters, tip-shape correction, uncertainty budget

1. Introduction

Nanomaterials are materials with size characteristics having one or more dimensions from 1 nm to 100 nm [1]. At the nanoscale, the materials present peculiar features which make them particularly interesting from different points of view. Nano-objects can be divided into (i) nanoplates, materials with only one

dimension in the nanoscale, (ii), nanofibers, objects with two dimensions in the nanoscale, *e.g.* nanotubes (hollow nanofibers), nanorods (solid nanofibers), nanowires (electrical conducting nanofiber), (iii) spherical or quasi-spherical nanoparticles (NPs), and (iv) complex shape nanoparticles with at least one dimension in the nanometer range [2]. Engineered nanoparticles are particles designed for specific purpose or function, and in the last decades there have been fast advances in the fundamental science and application of particles in products ranging from medical therapeutics to hybrid electronics. The NPs functional properties are strictly related to their sizes and morphological features. NPs can assume different shapes and textures of surfaces, depending on the fabrication methods, the precursors characteristics, and the physical/chemical interactions governing the synthesis process.

The great success of the nanotechnologies arises, on the one hand, from the necessity to miniaturization and, on the other, from the possibility to exploit the peculiar properties of structured matter at the nanometric level. In order to sustain the exponential growth of the nanoproducts, a considerable investment from industry, research institutes, national metrology institutes (NMIs), regulatory and standardisation bodies is needed. In particular, metrology supports nanosciences and nanotechnologies to develop samples and reference materials, reduce measurement uncertainty and define models and methodologies to support traceability of measurements on the nanometer scale [3].

In this context, nanometrology has a crucial role for producing nanomaterials and devices with a high degree of accuracy and reliability. Samples and reference materials are the crucial elements to guarantee the goodness of the measurements and to constitute a solid basis for manufacturing, within a framework of mutual recognition of certificates and products.

In order to achieve a desired functional property, nearly all nanotechnology applications require precise control of the dimensions [4]. In this framework, instrumentation, reference standards methods and protocols play a leading role to provide traceable measurements at the nanoscale [5]. Various material measures are available on the market [6], such as step-height and groove-depth standards, 1D and 2D gratings, linewidth standards, as well as several reference materials mostly based on spherical- or rod-shaped nanoparticles supplied in mono and/or multimodal dispersed suspensions. In laboratories and NMIs, standards and reference materials are continuously being developed [7] to meet the measurement needs, which now require new methods to fully characterize 3D shape and size at the nanoscale, for their effective dissemination at low cost.

Titanium dioxide (TiO_2) is a material widely employed in several fields, such as the production of varnishes and paints, food colouring, cosmetic dye and sun filter. Moreover, due to its photoinduced antibacterial and hydrophilic properties, it is used to produce self-cleaning surfaces [8], with commercial applications in automotive, medical equipments and protective clothing. Furthermore, because of its thermodynamic properties, TiO_2 is a semiconductor widely used as water splitting photocatalyst for hydrogen production [9]. Shape-controlled anatase TiO_2 NPs with different shapes (nanosheets and bipyramids) are obtained by tuning the parameters used in the synthesis [10,11]. TiO_2 anatase bipyramids and nanosheets are here studied as "candidate reference materials" for their critical sizes (CSs) [12].

In this paper, we discuss the 3D characterisation of the sizes of non-spherical anatase nanoparticles by means of a metrological Atomic Force Microscope (mAFM) [13]. These instruments make use of built-in interferometers to control or monitor the relative tip-sample movements when scanning the sample surface, thus ensuring a direct traceability to the realisation of the metre. Atomic Force Microscopes and Scanning Electron Microscopes (SEM) are defined as "direct techniques" providing direct measurements of the reconstructed sizes and morphologies of NPs, as opposed to non-imaging methods such as dynamic light scattering or centrifugal liquid sedimentation, which analyzed a large number of NPs but are not able to distinguish shapes and indirectly calculated the size.

Nevertheless, NPs with complex geometry represent a challenge with regard to AFM measurements, as the particular geometries of the nanoparticles highlight the limits related to the shape and finite size of the tip.

The AFM images show a geometric dilation due to tip size, which is furthermore evident in the presence of features with a high aspect ratio (HAR), and typically causes an overestimation of the external lateral dimensions of columns or steps and an underestimation of the internal ones in narrow grooves or valleys. Evidence of this geometric dilation is given in the AFM images of the complex-shaped NPs shown below, and they represent one of the main sources of error in their 3D AFM reconstruction.

The methodologies for the correction of this error are essentially based on the *a priori* characterization of the tip with reference samples and on blind reconstruction methods and algorithms [14,15,16,17,18]. The use of tip shape and size characterizers based on comb nanostructures with different spacing and width made it possible [19]; for example, to significantly reduce the error due to dilation in measuring linewidth standards [20] and in assessing tip quality for measuring the depth of very narrow trenches [21]. Among others, cylindrical nanostructures formed by the tobacco mosaic virus have also been studied as characterizers of AFM commercial standard tip [22,23]. To date, it is important to remember the very accurate method for the determination of the tip shape developed by PTB and based on the characterization of CD (Critical Dimensions) tips with a line width reference material [24] by means of CD-AFM measurements [25].

In this work, we describe the geometric model developed to correct this error in the AFM images of both TiO$_2$ bipyramids and nanosheets. Traceable and accurate quantitative measurement of some of their critical dimensions and shapes requires new methods to be implemented or translated into measurement applications on nanostructures of various shapes, at least for some characteristic measurands.

2. Materials and sample preparation

TiO$_2$ anatase nanoparticles are synthesised by hydrothermal methods using a 200 mL Teflon lined stainless-steel reactor. More specifically, nanosheets are obtained by using titanium butoxide as precursor in acid environment at 250°C for 24 h, as described in [10,11]. Truncated bipyramids are fabricated by using a complex of Ti(IV) with triethanolamine as precursor, in basic condition with a temperature of about 220°C, for 50 hours with a method similar to that reported in [26]. The post-synthesis treatment to obtain nanopowders is made by dialysis plus freeze-drying, in order to wash the NPs and eliminate the solvent [26].
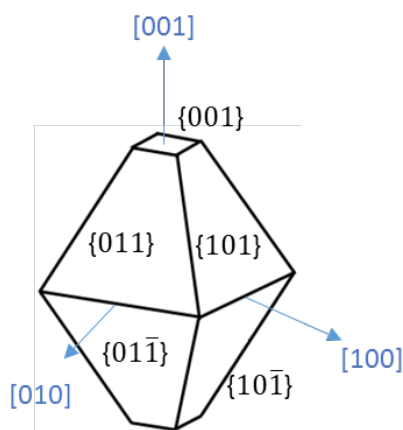

Figure 1. Equilibrium shape using Wulff construction for TiO$_2$ anatase crystals. Please note that in blue square brackets are reported the crystalline axes, while in curly brackets are given the anatase crystalline facets.

In Figure 1 is sketched the equilibrium shape using Wulff construction, that considers the surface energies of the crystal surfaces in the growth medium, for TiO$_2$ anatase crystals [27]. For the anatase phase, the

equilibrium shape is a slightly truncated tetragonal bipyramid enclosed by eight thermodynamically stable {101} facets and two {001} facets, with an interfacial angle ϑ = (68.3 ± 0.3)° from X-ray diffraction measurements [28].

By tuning the synthesis parameters, anatase crystals with different characteristics are obtained. In fact, the nanobipyramids have an elongated truncated tetragonal bipyramidal shape, while nanosheets are squashed along the [001] axis. This difference in shape is also expressed in the orientation in which they are arranged on the mica substrate, and consequently also in the way in which the CSs are calculated (paragraph 5.1).

For preparing the samples to be analyzed by mAFM, the nanopowder is dispersed into MilliQ water creating a suspension of 3 mg·L⁻¹, which is put in an ultrasonic bath for 5 hours for disagglomerating the NPs. For having a sample with isolated nanoparticles well dispersed onto an ultraflat substrate, a drop of 20 μL of suspension is deposited onto a freshly cleaved mica support, with 10 mm diameter, and let it dry to air and stabilize for at least 12 hours. The samples are then stored into plastic boxes and kept at a stable temperature of (20.0 ± 0.1) °C. Once the sample is mounted on the mAFM sample holder, few hours of thermal stabilization are needed before any measurement is taken.

3. Measurands, shape and texture descriptors

Pre-normative R&D and standardization works on specification, classification and characterization of nanoparticles have made available today several published standards [29]. These documents identify characteristics and measurement methods to ensure quality of products or conformity assessment, which means deciding whether a product or service conforms to specifications. A first step towards regulation is to describe clearly and unambiguously the object to be measured in a terminology which is consistent and understood by all. The properties of the nanoparticle that is regulated, *i.e.* 'quality characteristics', such as critical sizes, shape and texture descriptors, needs to be clearly defined [4].

In the following, CSs of anatase non-spherical nanoparticles are studied as measurands, together with some descriptors dependents by NPs shape and roughness parameters.
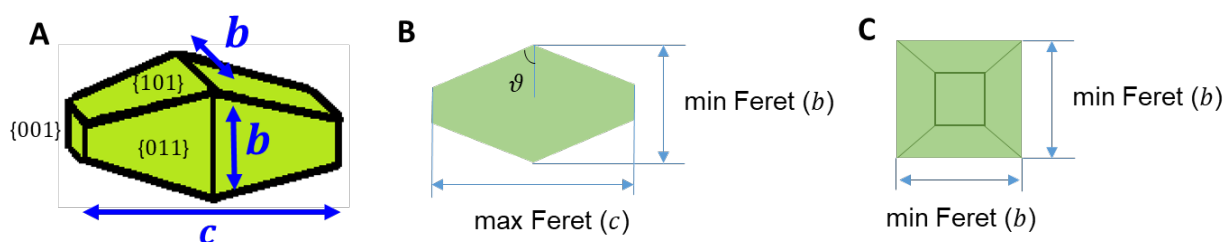
3.1 Bipyramids

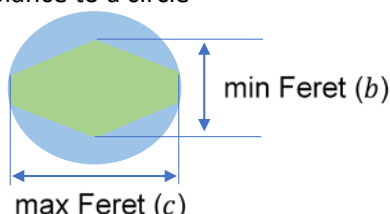*Figure 2. Not-to-scale 3D sketch of a TiO₂ bipyramid (A), side and top views (B), and front-view (C).*
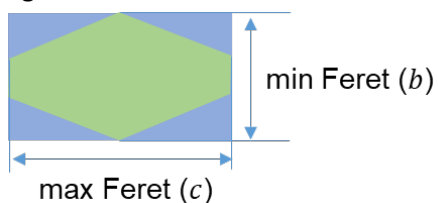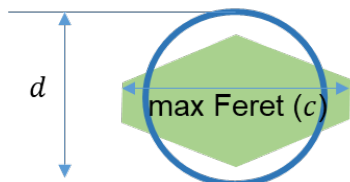
Figure 2 (A) reports a sketch of the TiO₂ anatase square base truncated bipyramidal NP with its crystalline facets, while Figure 2 (B) and (C) shows its size characteristics and the interfacial angle ϑ.
The size descriptors of TiO₂ bipyramids are b, that corresponds to the "breadth" of the particle, and c, which is the "length" of the nanoparticle, as reported in Figure 2 (B). Since the definition "length" c of the bipyramid is too generic and can lead to misinterpretations, later in the text we use the "Feret diameters". The Feret diameter is a measure of an object size along a specified direction, and it can be defined as the distance between the two parallel planes restricting the object perpendicular to that direction [30]. More specifically,

4

the "breadth" of the bipyramid is defined as "minimum Feret", while the "length" as "maximum Feret". We therefore choose to use Feret diameters, even if usually they are used for analysing images from electronic microscopes, in which a three-dimensional object is projected on a 2D plane.

The shape descriptors chosen for describing the bipyramids are the morphological parameters presented in Table 1. These parameters are some of the descriptors early reported in an interlaboratory comparison by TEM measurements performed on a different batch of anatase bipyramids [31]. It is worth noting that these shape descriptors make easier to identify and quantitatively compare the same characteristic from data taken by different instrumental techniques.

Table 1. Bipyramid shape descriptors.

Morphological parameters	Equation	Explanation
elongation	$El = \dfrac{\max Feret}{\min Feret}$	ratio of the maximum dimension to the minimum dimension
aspect ratio	$AR = \dfrac{\min Feret}{\max Feret}$	inverse of the elongation
projection area	$A = \pi \cdot \dfrac{\min Feret}{2} \cdot \dfrac{\max Feret}{2}$	bipyramid projection area calculated as elliptical area by using the two available CSs
roundness	$Rnd = \dfrac{A}{\pi \left(\dfrac{\max Feret}{2}\right)^2}$	ratio of the bipyramid area to the circular area, describes the resemblance to a circle
bulkiness	$B = \dfrac{A}{\max Feret \cdot \min Feret}$	ratio of the bipyramid area to the rectangular area defined by the dimensions, describes the resemblance to a rectangle
compactness	$cmp = \dfrac{d}{\max Feret}$ $= \dfrac{\sqrt{\dfrac{4 \cdot A}{\pi}}}{\max Feret}$	ratio of the equivalent circular diameter to the dimension 'c', describes the degree to which the diameter of the particle is similar to that of circle with the same area

3.2 Nanosheets

In Figure 3(A) is reported a 3D sketch of a TiO₂ nanosheet, which highlights the presence of a large {001} crystalline facet. The nanosheets have also a bipyramid shape but with a truncated "length" along the [001] axis, now called height h, and a square base of side l, as illustrated in Figure 3 (B, C).
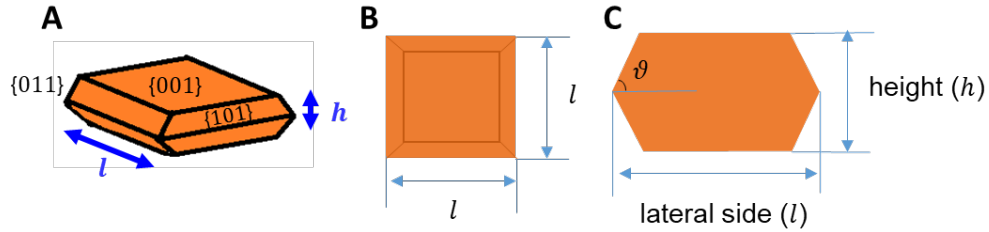

Figure 3. Not-to-scale 3D sketch of a TiO₂ nanosheet (A), its view from above (B), and side-view (C).

For characterizing nanosheets with surface texture descriptors, the roughness of the {001} exposed crystalline facet, either by profile [32] and areal texture parameters [33], is quantitatively studied.

We decide to study the roughness of a candidate reference nanoparticle because it is important to have a material used as parameter reference. In fact, at the nanoscale level, roughness is very important in the AFM study on various fields, such as in tribology, in the correlation between friction coefficient and roughness height-amplitude parameters [34], and in material science, in the study of the performance and behavior of a material to a specific treatment [35].

The roughness of anatase TiO₂ is extensively studied in literature for polycrystalline films, which rms (Rq) values range from a few to tens of nanometers depending on the sample thickness [36]. A functional characteristic of TiO₂ films depending on nano-roughness is the wettability, that strongly depends on texture and size of crystalline domains [37].

In studying the surface roughness and texture of nanosheets, we make use of amplitude parameters, calculated on the length/size of the profile/area of the nanosheet surface without further cut-off filters, and a hybrid parameter, which calculation is based on local Z-slope. For comparison, both profile roughness R and areal texture S parameters texture are reported.

The Ra and Sa express the arithmetical mean of the heights of a line profile or a surface, while the root mean square of the height values $R_q = \sqrt{\frac{1}{L}\int_0^L |Z^2(x)|dx}$ and $S_q = \sqrt{\frac{1}{A}\iint_A |Z^2(x,y)|\,dxdy}$ are more sensitive than average parameters to the presence of peaks and valleys, and are therefore suitable to quantify localized surface modifications. These last are also highlighted by the maximum height Rz and Sz, as the sum of the highest peak and the deepest valley.

The roughness skewness Rsk and Ssk rely on the asymmetry of the z-heights distribution, while the roughness kurtosis Rku and Sku measure the sharpness of the roughness profile.

The hybrid parameter present in this paper is the surfaces area ratio Sdr, that expresses the increment of the interfacial surface area (the real surface) relative to the area of the projected plane (that is the reference planar surface).

4. Instrumentation and measurements

AFM, SEM, TSEM (Transmission-mode Scanning Electron Microscopy), and TEM are defined as "direct techniques", because they permit a direct measurement on shape and size of NPs, nanostructures, and nanomaterials. While electron microscopes are traced by means of calibrated standards like 2D gratings/grids, metrological AFMs are directly traceable to the SI, through built-in interferometers.

INRiM mAFM is a custom-made instrument with a multimode AFM head arranged on a sample-moving mechanical structure; the microscope is equipped with on-board metrology to monitor relative tip-sample displacements and to guarantee the traceability of the measured dimensions.

The instrument may operate with two distinct XY scanning devices, the first with separate stages with a working range of about (30 μm x 30 μm), and the second a working field of about (100 μm x 100 μm), both coupled to the optics of a laser interferometer to control XY displacements. The Z stage is based on a piezoelectric translator with a 2 μm working range; it is calibrated in situ with an interferometric device [38]. The ambient conditions are kept within (20.0 ± 0.1) °C with a relative humidity (50 ± 10) %.

Measurements are carried out in non-contact mode using commercial silicon tips [39], which nominal characteristics are a radius of 8 nm, a force constant of 5 N·m^{-1} and a resonance frequency of 160 kHz. As a common practice in our laboratory, standard tips were used for such a demanding measurement runs. No high-resolution tips were used till now. Assuming the nominal half-angle of 20 ° at the tip apex and the lying angles of the bipyramidal surfaces and nanosheets, a small area of interaction between the tip and the surface is expected when scanning the square base of the bipyramids along the fast X-axis of the image, while a large area of interaction can occur at the edges of the nanosheets and bipyramids lying on a {101} facet, thus causing an uncertainty in the edges of the profile that has been addressed by the geometric approaches described below.

Both the NPs types were imaged in two different periods, analysing about half NPs for one month in summertime and the other half for one month in the following winter; three bipyramids and three nanosheets specimens, prepared as described in section 2, are measured. The recorded mAFM images have sizes from (300 nm x 300 nm) to (500 nm x 500 nm) with a resolution of (512 pixels x 512 pixels). Each topography measured (106 images for nanobipyramids and 100 images for nanosheets) is centered on a single nanoparticle, to determine sizes, shape and texture for each individual NP, thus achieving a good enough data set.

5. Methods and Results

With quasi-spherical nanoparticles well dispersed onto an ultra-flat substrate, the AFM-based measurement of the mean diameter is easily performed by determining the top-height of the NP cross-section profile [40], whereas with non-spherical NPs, size and shape measurements by AFM are trickier, due both for the finite size of the tip and for the geometry of the NPs. Therefore, geometric approaches have been developed for determining the sizes of bipyramids and nanosheets.

5.1 Image processing for CSs reconstruction of non-spherical NPs

AFM images of single non-spherical NPs deposited onto freshly cleaved mica are firstly pre-processed by means of the Scanning Probe Image Processor (SPIP) software [41]. The image is levelled to eliminate the inclined plane between the tip scanning plane and the areas of the image in correspondence of the flat mica substrate.

If necessary, the image is rotated in the XY plane in order to have (i) the bipyramid along the Y direction of the image, or (ii) the nanosheet lateral dimension parallel to the X axis.

Then, images are processed by our own soft-tools developed with MATLAB to implement the geometric models for determining the CSs of the bipyramids and of the nanosheets. All data and profiles from the processing of single nanoparticles are saved in into matrixes, by which further or comparative steps, *e.g.* in a spreadsheet, are easily available.

5.1.1 Bipyramids
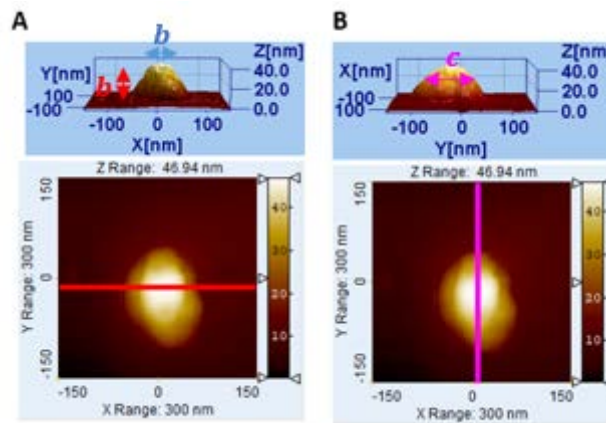
Figure 4. 2D and 3D topographies of a nanobipyramid by mAFM. Determination of (A) 'b' and (B) 'c' sizes.

Figure 4 displays a raw topography centered on a single bipyramid as reconstructed by the mAFM. The 3D images on top highlight the sizes to be measured, namely the minimum Feret b and the maximum Feret c of the bipyramid.
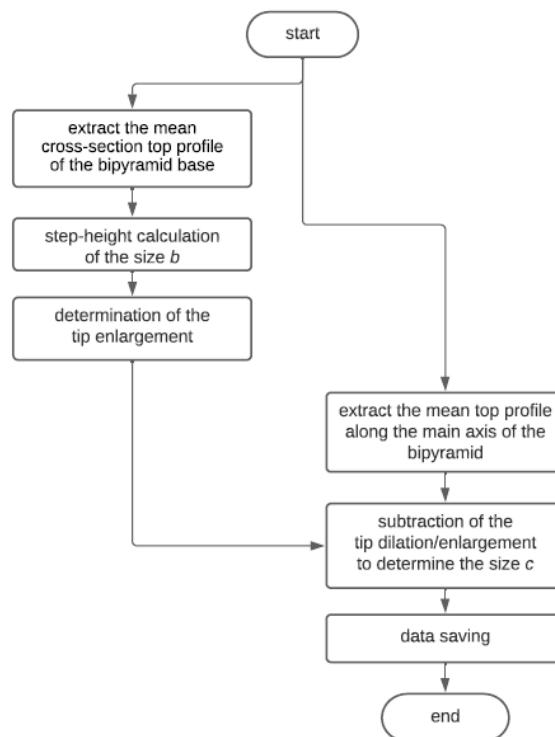

Figure 5. Flowchart describing the main steps in the calculation of the bipyramid critical sizes.

8

Our geometric model is based on two assumptions: (i) the bipyramid, due to its intrinsic nature, has a square base (paragraph 2), and (ii) the tip has an isotropic shape at the apex. The tip has an anisotropic shape (trihedral) if we consider its global size (of the order of tens of micrometres), but at its very end of tens of nanometers at the tip apex, its shape is assumed isotropic.

From the analysis of the cross-section top profile along the X axis are extracted (i) the step-height from the mica substrate to the top height (size b) in correspondence of the bipyramid base and (ii) the tip enlargement profile. Instead, the max Feret c is obtained by subtracting the tip enlargement profile from the cross-section top profile along the Y axis.

The process outlined by the flowchart in Figure 5 is implemented and tested in our soft-tool. To let the operator know if the process steps in the calculation of bipyramid CSs are properly made, the "A" to "E" profiles in Figure 6 are subsequently calculated and displayed.
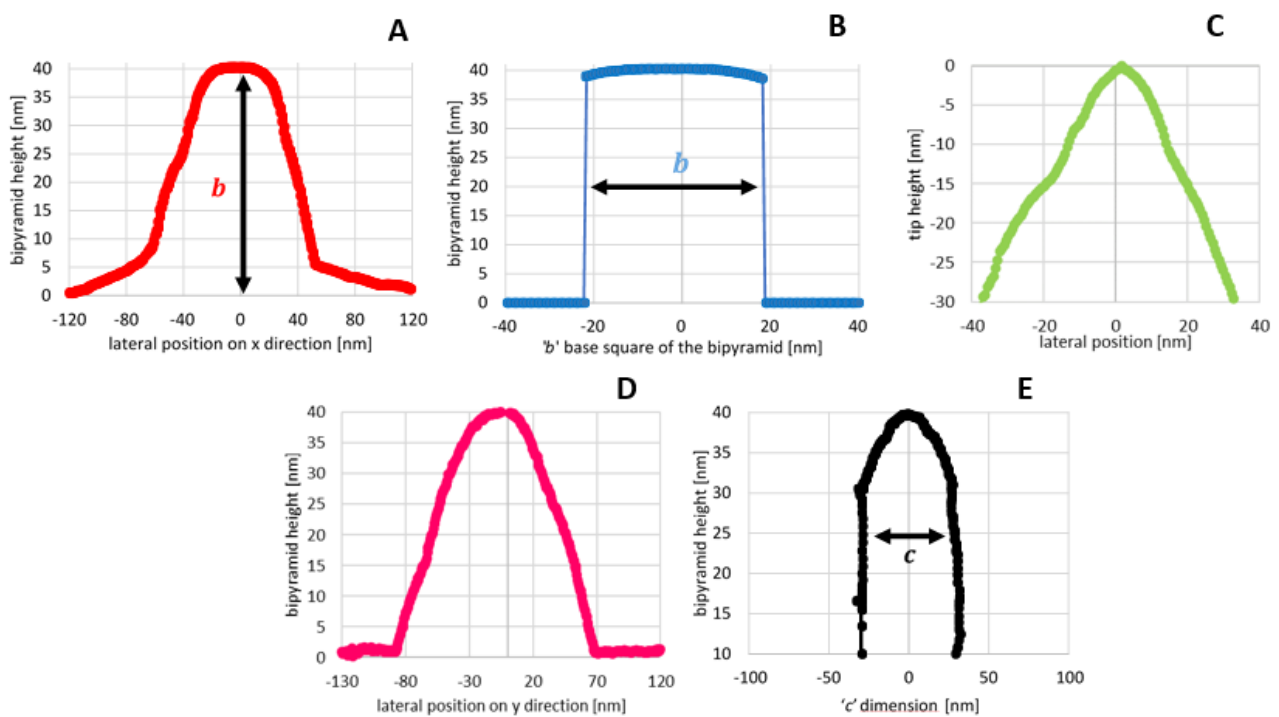
Figure 6. Process steps in the determination of bipyramid critical sizes:
(A) Mean cross-section top profile at the bipyramid base;
(B) The size b of the square base of the bipyramid;
(C) Tip enlargement as estimated by A and B;
(D) Mean longitudinal profile along the axis of the bipyramid;
(E) The size c as obtained by subtracting C from D.

After tilting removal and rotation of the image to have the NP's axis along the Y-axis of the image, the maximum z-height of the NP's topography is searched along the X-lines of the image in order to find and build the top cross-section profile of the NP. To minimize the influence of spikes, five X-lines around the maximum z-heights of the image are averaged in a single profile (Figure 6 (A)), from which the size b, i.e., the step-height of the profile, is calculated according to the ISO 5436 [42].

Since the bipyramids have a square base, a length b of the profile at the top of the cross-section (Figure 6 (B) is taken while all the other parts of the cross-section are set equal to the mean z-height of the baseline (clean mica surface) if not yet removed its z-offset. In this way, the profile of the square base of the bipyramid not dilated by the tip geometry is achieved.

This geometric approach also permits the determination of the tip enlargement (Figure 6 (C)). To depict it, the length b of the profile in correspondence of the bipyramid base in Figure 4 (A) is simply deleted; in other words, from the profile in Figure 4 (A) the base of the square b is not considered.

After that, the longitudinal section profile along the axis of the bipyramid (Figure 6 (D)), *i.e.* the Y-axis of the image, is extracted. Again, five Y-lines of the image are averaged to minimize noise and spike effects. In order to obtain the size c (Figure 6 (E)), the tip dilation profile (Figure 6 (C)) up to the z-heights of the bipyramid terminations is subtracted to the mean longitudinal profile (Figure 6 (D)).

Once more, one has to consider the inclined lying of the bipyramid on the mica substrate. Since the bipyramid lays on a $\{101\}$ facet (Figure 7 (A)), the measured size b_{meas} of the base is corrected according to sine of the interfacial angle of the anatase crystal, which value is ϑ = (68.3 ± 0.3)° from crystallographic measurements. The lying of the bipyramid is confirmed by AFM measurements of the angle between the ascent segment and the top constant segment of the bipyramid profile along the Y scan axis direction, resulting in 2ϑ = (136.9 ± 10.2)° as (mean value ± standard deviation).

Similarly, the measured c_{meas} is corrected for the cosine of the angle γ, as reported in Figure 7 (B).

(A)   (B)
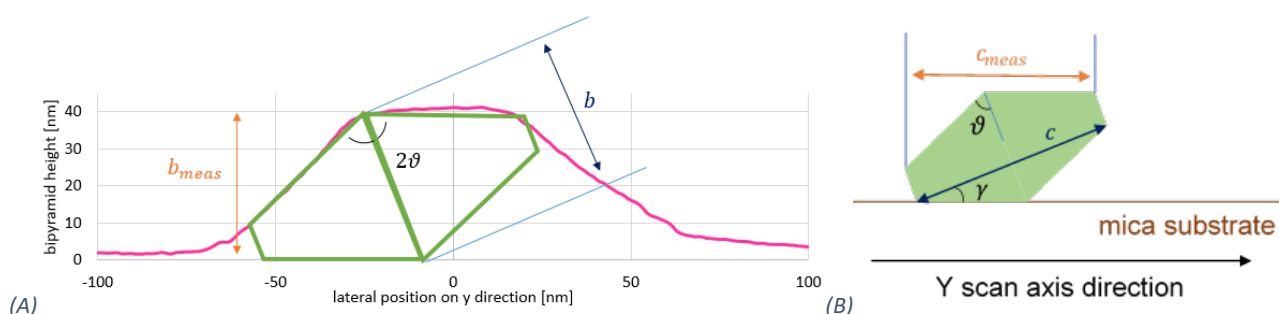
Figure 7 (A) Profile along the Y scan axis direction with a side-view sketch of bipyramid laying onto substrate highlighting the correction of the size 'b'. (B) Not-to-scale side-view sketch of nanobipyramid laying onto mica substrate substrate highlighting the correction of the size 'c'.

5.1.2 Nanosheets

These anatase nanoparticles have a truncated tetragonal bipyramidal shape squashed along the [001] axis; the peculiarity of these NPs is a height much smaller than the lateral size of the two end $\{001\}$ facets, one exposed and the other laying onto the mica substrate. Figure 8 displays a topography centered on a single nanosheet.
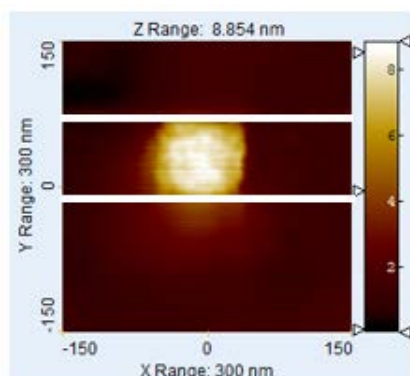
Figure 8. 2D topography of a nanosheet by mAFM.

The geometric model for processing the nanosheets is outlined on the sketch in Figure 9 and in the flowchart in Figure 10. The blue line represents the mean cross-section profile of the nanosheet, which is calculated as the mean of the X-line profiles within the white lines in Figure 8, *i.e.*, the part of the image with the exposed facet area of the nanosheet.

Figure 9. Not-to-scale sketch illustrating the geometric approach to determine the nanosheet sizes. The blue line indicates the mean cross-section profile, the orange figure pictures a side view of a nanosheet, and the rows represents the segments involved into the geometrical analysis.
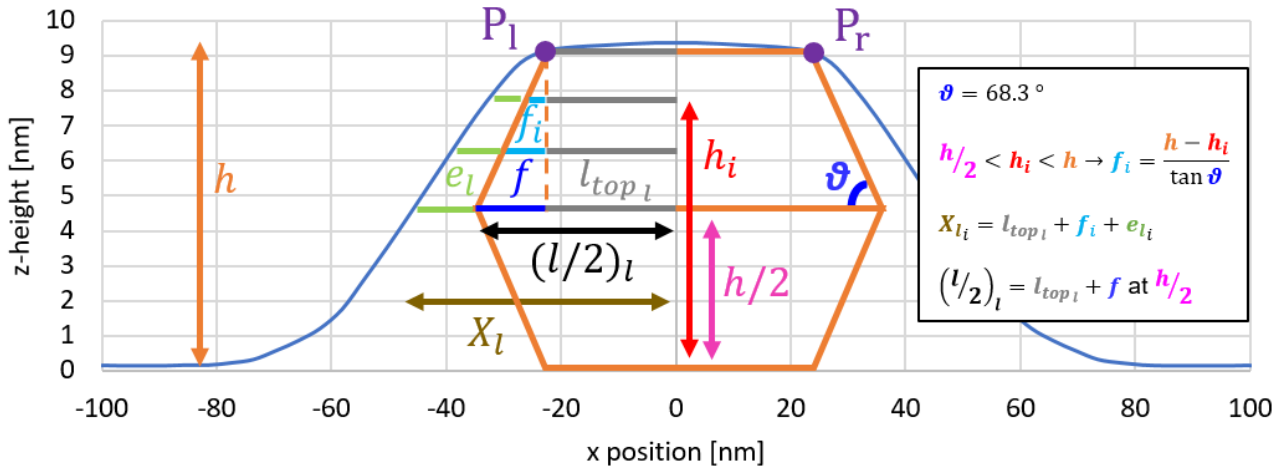
In order to find the critical sizes, the edge points P_l and P_r are determined as the intersection of linear regression lines fitting parts of the top and of the left/right sidewalls of the mean cross-section profile. The fitting line at the top part of the profile considers all points with Z-heights from 90% to 100% of the maximum height of the profile, while the points with heights from 60% to 80% are taken for the fitting lines of the left/right sidewall parts of the profile. A repeatability better than 95% has been determined for the edge points P position, varying by 10% the Z-heights of the left/right sidewall to be taken for the fitting lines.

The height h of the nanosheet is therefore assumed as the mean of the Z-heights of the two edge points P, providing that the mean height of the profile in correspondence of the mica substrate is at zero height. The size of the top base of the nanosheet l_{top} is given by the lateral (X) distance between the edge point and the center of the nanoparticle.

To further check the consistency of these sizes, the segment $f_i = \frac{h-h_i}{\tan \vartheta}$ is calculated at various heights h_i between $h/2$ and h, and the left lateral size $(l/2)_l$ of the nanosheet is obtained by the sum of $l_{top_l} + f$ at the half-height $h/2$. Again, use is made of the known interfacial angle $\vartheta = (68.3 \pm 0.3)°$.

Thus, the left side tip enlargement e_l at various heights can be obtained as the difference between the measured lateral position along the cross-section profile $X_{l\,i}$ and the sum of the segments l_{top_l} and f_i.

The same calculation is done for the right side of the profile, for obtaining the right lateral side $(l/2)_r$ and the tip enlargement e_r at the right side of the nanosheet.

The lateral dimension l is defined as the sum of $(l/2)_l$ and $(l/2)_r$, while the tip enlargement profile is obtained by the sum of the segments $e_{l\,i}$ and $e_{r\,i}$ at the same height h_i.

In addition, image processing and calculation of sizes are repeated for the Y-axis cross section profile of the nanosheet. Therefore, the height h and size l reported in section 5.2.2 are the average values of those calculated from the X and Y cross-section profiles of the nanosheet.
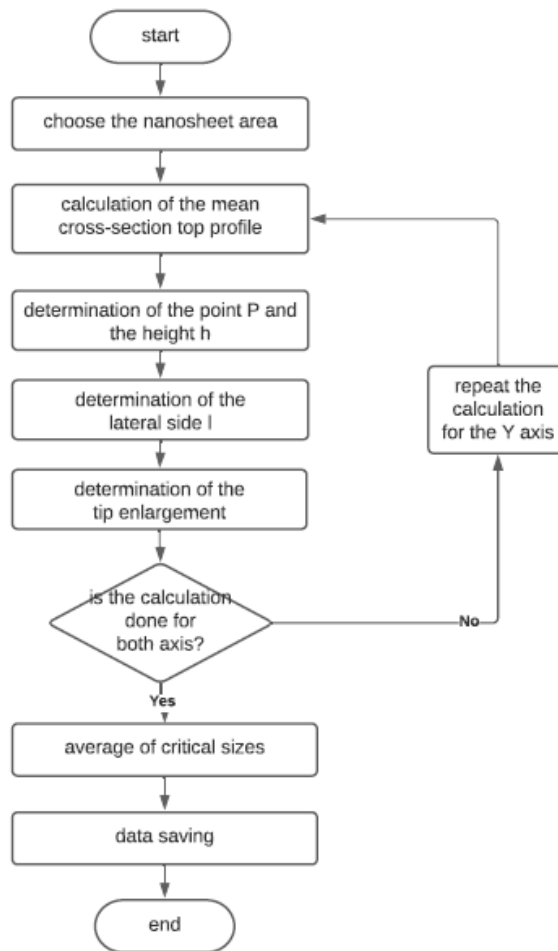
Figure 10. Flowchart describing the data processing in the calculation of the nanosheet critical sizes

Figure 11 compares the tip enlargement for X and Y profiles obtained by the analysis of a nanosheet, showing a good agreement between the two profiles. This figure supports the assumption of AFM tips with an isotropic shape at the apex, also assumed with the AFM images of the bipyramids (section 5.2.1).

It is worth noting that a large interaction area between tip and surface is expected when profiling the edge of the nanosheet. Thus, the reconstructed tip enlargement profile (that we obtain with our geometrical approach) reflects such a lateral tip-sample interactions preventing a proper reconstruction of the tip shape. For comparison, the nominal radius of curvature of the tip shape has been added in Figure 11.
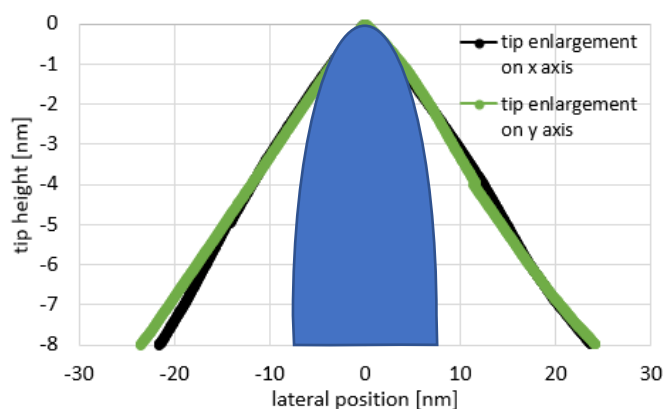
Figure 11. Tip enlargement profiles on X and Y directions obtained by analysing an anatase nanosheet.
The blue shape represents a tip with nominal radius of 8 nm.

A final consideration that can be made is that the advantage of using such a geometrical model is to quantitatively analyze selected measurands of isolated non-spherical NPs in a robust, repeatable and fast way. Since the geometrical method can be easily modified for determining some crucial sizes of isolated NPs with other non-spherical geometries, such as nanorods and/or nanocubes, therefore also the soft-tools can be easily modified.

5.2 Results

Critical sizes, shape descriptors and surface texture of anatase TiO_2 nanoparticles having the form of bipyramids and nanosheets are summarized below in tables and hystograms providing useful data of sizes, shapes and finiture of these monomodal NPs with complex geometry. Note that the numerical results are reported as (mean value ± standard deviation).

A "candidate reference material needs to be investigated to determine if it is sufficiently homogeneous and stable with respect to one or more specified properties" [43]; as shown by the results given in the following sections, the NPs deposited into mica and stored at stable environmental temperature shows good stability of the measurands over the time.

5.2.1   Bipyramids

The analysis on 106 images (106 bipyramids) gives the sizes b = (43.2 ± 3.4) nm and c = (58.2 ± 5.2) nm. These results are in good agreement with the analysis performed in a similar sample, but of a different batch [44]. Figure 12 shows histogram distribution for the two bipyramids measurands. It is worth noting that both the bipyramids CSs have a dispersion that is narrow and monomodal, and so b and c dimensions have resulted sufficiently homogeneous, to apply as candidate reference material.
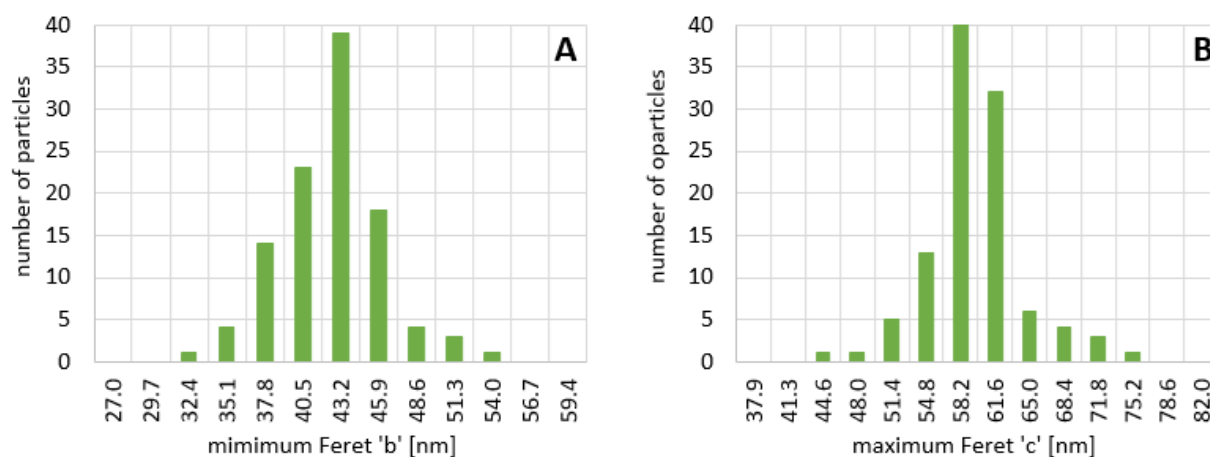
Figure 12. Histograms on bipyramids critical sizes: (A) min Feret 'b' and (B) max Feret 'c'.

In Table 2 are reported the shape descriptors calculated as described in Table 1 for all 106 bipyramids. It can be noticed that these nanoparticles resemble for the 80% to a rectangular area (bulkiness ~ 0.8), for the 80% to a diameter of a circle with the same area (compactness ~ 0.8), and they resemble for 70% to a circle (roundness ~ 0.7). Moreover, an elongation ~ 1.4 (and so and aspect ratio of about 0.7) indicates a bipyramid with a perfect truncated shape [26], so the study of these two descriptors is very important to understand the quality of the batch synthetized. In fact, through these shape descriptors we are able to know if bipyramids from different batches can be able to apply as reference materials.

Table 2 Shape descriptors calculated for 106 bipyramids. Values are reported as (mean value ± standard deviation).

Descriptor		Unit	AFM measurements
projected area	A	[nm^2]	1969.2 ± 216.6
aspect ratio	AR	-	0.7 ± 0.1
elongation	El	-	1.4 ± 0.2
roundness	Rnd	-	0.7 ± 0.1
bulkiness	B	-	0.8 ± 0.1
compactness	cmp	-	0.8 ± 0.1

5.2.2 Nanosheets

About 100 nanosheets are imaged with the mAFM, and then analyzed as described in section 5.1.2.

The results, displayed in Figure 13, are h = (9.3 ± 1.4) nm and l = (75 ± 26) nm. Results of the mAFM measurements are well in agreement with those from the same batch analyzed by means of TSEM, by which height value h = (9.4 ± 1.6) nm and lateral values l = (75 ± 25) nm were reported [11]. Please note that all the values above are given as (mean value ± standard deviation).

As shown in Figure 13, the distributions of both the CSs of the nanosheets are monomodal, but while the height h has a narrow dispersion, the lateral dimension is more dispersed due to the grow of the crystals during the synthesis. For this reason, only the height h can apply as a reference size at the nanoscale.
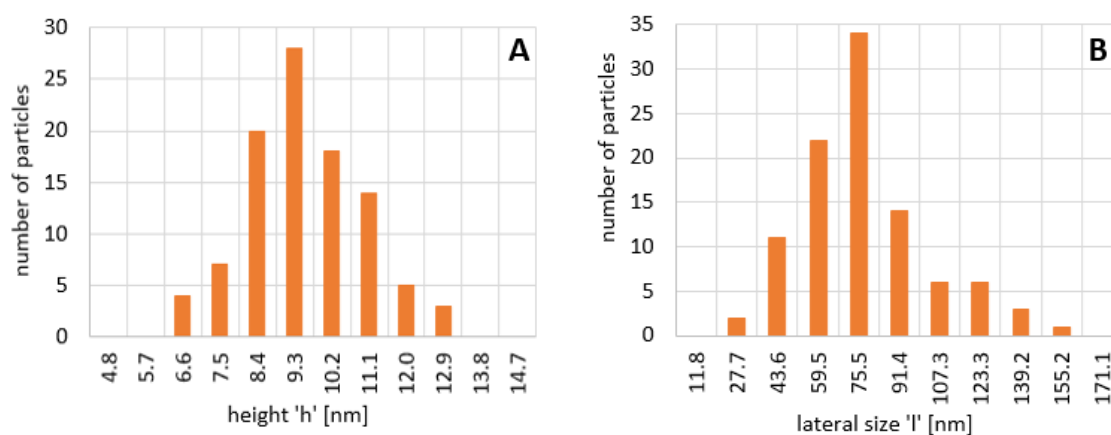
Figure 13. Histograms on nanosheets critical sizes: (A) height 'h' and (B) lateral dimension 'l'.

In addition, a quantitative characterisation of the surface texture parameters on the nanosheets {001} exposed facet and on mica substrate is presented in Table 3 and Table 4. To determine these parameters, the mAFM image of each nanosheet is tilted to minimize the inclined plane of the image. After that, an area and a profile are extracted both onto mica substrate and in the centre of the nanosheet, for analysing only the {001} facet.

Moreover, a line-wise offset correction (LMS fit of degree zero) is made for each area extracted using SPIP tool. Line-wise distortions are typical scanning artefact like steps between subsequent scan lines occurring when changing from outward to inward direction of the tip scanning or by some tip contaminations along scanning.

Table 3. Roughness parameters (mean value ± standard deviation) calculated from 100 nanosheets.

Descriptor	Profile	
	mica	nanosheet
Ra [nm]	0.14 ± 0.04	0.34 ± 0.09
Rq [nm]	0.17 ± 0.05	0.41 ± 0.10
Rz [nm]	0.63 ± 0.25	1.44 ± 0.44
Rsk	0.11 ± 0.63	-0.59 ± 0.56
Rku	2.53 ± 0.72	2.56 ± 0.69

Table 4. Areal texture parameters (mean value ± standard deviation) calculated from 100 nanosheets.

Descriptor	Areal	
	mica	nanosheet
Sa [nm]	0.14 ± 0.04	0.34 ± 0.07
Sq [nm]	0.17 ± 0.05	0.42 ± 0.09
Sz [nm]	1.03 ± 0.40	2.08 ± 0.61
Ssk	0.10 ± 0.52	-0.60 ± 0.51
Sku	3.18 ± 0.89	3.05 ± 0.72
Sdr [%]	0.05 ± 0.03	0.18 ± 0.10

In Table 3 and Table 4 are compared the parameters calculated on the NPs and substrate surfaces, and it can be noticed that the profile roughness parameters Ra and Rq are practically the same of the areal parameters Sa and Sq, since both are isotropic surfaces.

Mica has a Rq (rms) roughness of about 0.2 nm, as reported in literature [45], while the nanosheets' surface presents a larger roughness also in agreement with those in the range of 0.22 nm to 0.88 nm given for anatase single crystals [46].

Compared to average values, the rms Rq and Sq values are more sensitive to the presence of local surface peaks and valleys, which are even more highlighted by the Rz and Sz peak parameters. To understand if these surface variations are peaks or valleys, that can be broad or sharp, skewness and kurtosis parameters are investigated.

The skewness Rsk and Ssk rely on the asymmetry of the profile and areal texture. Skewness with positive or negative values means that peaks or valleys are present, while a null (zero) skewness characterize a symmetrical texture around the mean plane.

The kurtosis Rku and Sku measure the sharpness of the surface texture. A kurtosis greater or lower than three represents sharp or broad textures, while if equal to three the height distribution is gaussian, with the coexistence of sharp and indented portions.

With the nanosheets, the kurtosis in Table 3 and Table 4 is around three for areal parameters (normal distribution of peaks and valleys), while the profiles show a presence of broader peaks and valleys.

Skewness is slightly positive for the mica substrate. For the nanosheets, the skewness is slightly negative, confirming the presence of valleys, so this parameter describe the possible presence on the anatase crystals of (i) electronic defects [10,47], or (ii) lattice vacancies, as presented in literature from STM images [48].

The surfaces area ratio Sdr is an index of the "complexity" of the surface. Sdr = 0 % for a totally flat surface, since the real surface and the reference area are the same, while is greater if gradient components of several degrees are present. The mica area has a value near 0 %, while this value is slightly greater for the nanosheets, that indicates, together to Sa and Sq, that the nanosheets have a roughness low enough to be used as reference in nanometrology.

5.3 Uncertainty budgets on CSs

In this section the uncertainty budgets for the mean values of the nanoparticle measurands are presented in accordance with the GUM [49].The intent is to estimate the different sources of error for obtaining a more reliable and consistent result, with a measurement model that considers any systematic errors and the uncertainty associated with their corrections.

The budgets are reported in the form suggested by the guide EA-4/02 [50], with the contribution to uncertainty quantity X_i and its estimate x_i, the standard uncertainty of the estimate $u(x_i)$, the sensitivity coefficient c_i, that describes the extent to which the source of uncertainty influences the overall uncertainty, the uncertainty contribution to the estimated quantity $u_i(y)$, which gives the final contribution from a given source of uncertainty to the overall uncertainty. Please note that N indicates a normal probability distribution, that is present when the source of uncertainty has a gaussian distribution; R indicates rectangular distribution, if the source of uncertainty has the same probability of being contained within an interval. Furthermore, the combined standard uncertainty $u_c(y)$ is reported; it is the overall uncertainty calculated by combining the individual values $u_i(y)$ according to the law of propagation of uncertainty. Finally, the expanded uncertainty U is reported, by multiplying the combined standard uncertainty per the coverage factor k.

In all budgets the uncompensated thermal drifts are not considered since the contribution due to the temperature readings and to the coefficient of thermal expansion of the anatase TiO₂ is negligible.

5.3.1 Bipyramids

Table 5 reports the uncertainty budget of the bipyramid b measured as thickness of the X-axis cross-section profile. The adopted model equation is $b = C_z \cdot b_m + \delta_{pl} + \delta_{lev} + \delta_{int} + \delta_{lay} + \delta_{str}$.

Measurement repeatability b_m is evaluated from the standard deviation of the mean thickness from 106 bipyramids; this term also considers the rotation of the structures.

The C_z factor considers (i) the calibration, that takes into account the interferometric calibration of the z axis including Abbe error ($0.5 \times 10^{-3}L$, where L is the vertical displacement of the stage), optical non-linearity (1 nm), dead-path (0.5 nm) and cosine errors ($0.5 \times 10^{-4}L$), (ii) the profile noise (0.3 nm), measured as Rq of mica along X-direction profile, and (iii) the resolution of the D/A converter (0.1 nm) on the piezoelectric stroke of 2 μm; this last contribution is negligible. Note that the previous values reported in brackets refers to normal and rectangular distributions resulting in a combined standard uncertainty of the C_z factor of $1.7 \cdot 10^{-2}$, including constant and proportional terms calculated at the nominal b size of about 40 nm of the bipyramid base.

Table 5. Uncertainty budget of the bipyramid 'b' size.

quantity X_i	estimate x_i	standard uncertainty $u(x_i)$	unit	probability distribution	sensitivity coefficient c_i	standard uncertainty $u_i(b)$ [nm]
repeatability b_m	43.2	0.3	nm	N	C_z	0.3
C_z factor	1	0.02	-	N	b_m	0.7
reference plane δ_{pl}	0	2.0	nm	R	0.58	1.2
levelling δ_{lev}	0	0.3	nm	R	0.58	0.2
tip-sample-substrate interactions δ_{int}	0.4	0.2	nm	R	0.58	0.1
correction for bipyramid laying δ_{lay}	3.5	1.4	nm	R	0.58	0.8
mechanical drifts δ_{str}	0	0.6	nm	R	0.58	0.3

combined standard uncertainty $u_c(b)$	**1.7**
degrees of freedom ν_{eff}	90
coverage factor k	2.025
expanded uncertainty $U(b)$	**3.4**

The reference plane correction δ_{pl} assumed with zero mean value refers to the error in the definition of the substrate plane. Since b is defined as top-height measurement, one has to be careful to define the height of baseline, *i.e.* the mica surface. This contribution has been evaluated by repeating five times the baseline definition in the same image for ten different images.

The levelling of the substrate δ_{lev} is evaluated through a method that considers the variation of the thickness value b after the tilting of the substrate orientation for an angle of 1°. More precisely, from a position in which the substrate is levelled, is studied the thickness variation by varying the angle from -0.5° to 0.5°.

The correction δ_{int} due to the interactions between the tip, the sample and the substrate is assumed with an uncertainty contribution calculated from the maximum error. Tip-sample and tip-substrate interactions are elastic terms, while sample-substrate deformation is elastoplastic. Note that tip-substrate and tip-sample deformations are calculated by using the Hertzian model [51] considering the silicon tip apex a sphere with a radius of 8 nm, the mica substrate a plane, and approximating the NP resting on mica to a cylinder with a radius equal to the bipyramid min Feret and a length equal to the max Feret. To note that these negligible elastic interactions (∼ 0.02 nm) compensate to each other.

The adhesion interaction between the bipyramid and the mica is calculated by means of the Chaudhury model [52], which describes the interaction between a cylinder (the bipyramid) and a plane (the mica), obtaining a deformation δ_{int} = 0.4 nm.

Please note that these models do not considers complex geometries, but we have reasonably approximated the bipyramid by using its CSs in order to estimate the entity of the interactions. In fact, the contributions due to tip-sample-substrate interactions are not so relevant, since both anatase TiO_2 NPs and Si tip are stiff/hard materials.

Note that the parameters used in the calculations are (i) the elastic moduli E_{TiO_2}= (237 ± 3) GPa [53], E_{Si} = (170 ± 5) GPa [54], E_{mica} = (190 ± 20) GPa [55], and (ii) the Poisson ratios v_{TiO_2}= (0.27 ± 0.02) [56], v_{Si}= (0.22 ± 0.01) [57], and v_{mica}= (0.25 ± 0.01) [58].

The bipyramid laying onto mica substrate is corrected as described in section 5.1.1, while the uncertainty of the correction is evaluated by varying the interfacial angle ϑ.

The uncompensated mechanical drifts refer to the straightness, that reports the variation of Rt profile along Y axis onto mica before and after line-wise correction tool. It is assumed with a zero mean value and an uncertainty equal to the straightness, as mentioned above.

Table 6. Uncertainty budget of the bipyramid 'c' size.

quantity X_i	estimate x_i	standard uncertainty $u(x_i)$	unit	probability distribution	sensitivity coefficient c_i	standard uncertainty $u_i(c)$ [nm]
repeatability c_m	58.2	0.5	nm	N	C_X	0.5
C_X factor	1	0.02	-	N	c_m	1.3
correction for bipyramid laying δ_{lay}	4.5	1.5	nm	R	0.58	0.9
tip dilation size δ_{dil_b}	43.2	1.7	nm	N	1	1.7
tip dilation wear δ_{dil_w}	0	2.8	nm	R	0.58	1.6

combined standard uncertainty $u_c(c)$	**2.9**
degrees of freedom v_{eff}	115
coverage factor k	2.025
expanded uncertainty $U(c)$	**5.8**

Table 6 reports the uncertainty budget of the bipyramid c size, which model equation is $c = C_X \cdot c_m + \delta_{lay} + \delta_{dil_b} + \delta_{dil_w}$.

The repeatability considers the standard deviation of the mean of the 106 bipyramids analyzed.

The X-size factor C_X deals with (i) the uncertainty of the image side, that consider the interferometric calibration of the x axis, (ii) the pixel size (1 nm), depending by the resolution and dimensions of the images, and (iii) the resolution of the D/A converter (<0,1 nm), this last negligible. Note that the values reported in brackets refers to normal and rectangular distributions resulting in a combined standard uncertainty of the C_X factor of $2.3 \cdot 10^{-2}$, including constant and proportional terms calculated at the nominal c size of about 60 nm of the bipyramid length.

The uncertainty of the correction for bipyramid laying δ_{lay} is evaluated by varying the interfacial angle ϑ.

The uncertainty of the tip dilation correction takes into account (i) the uncertainty of the size b $\delta_{dil\,b}$, from which it is calculated according to the assumptions made in the geometrical approach, and (ii) the tip wear $\delta_{dil\,w}$, evaluated through the analysis of the lateral enlargement of the dilation profile taken by the same tip on subsequent images. In fact, the size c is calculated by taking the average profile Y and subtracting the tip, whose geometry depends on size b. At a height of 20 nm, the tip dilation has a value of about 10 nm, and his uncertainty contribution is evaluated as rectangular maximum error.

5.3.2 Nanosheets

The model equation of the nanosheets height is $h = C_z \cdot h_m + \delta_{pl} + \delta_{lev} + \delta_{int} + \delta_{lay} + \delta_{str}$, and in Table 7 the uncertainty budget table is given.

The repeatability, Z-heights, substrate levelling, reference plane, and uncompensated drifts uncertainty sources are evaluated as reported for the budgets previously described in Table 5.

The tip-substrate interaction is equal to that reported in section 5.3.1, while the elastic tip-sample interaction is $\alpha_{tip-sam}$ = 0.02 nm both in the case in which is considered the interaction between a spherical tip and a nanosheet considered as (i) a plane or (ii) a cylinder with a very large diameter.

Sample-substrate adhesion are equal to $\alpha_{sam-sub\;\text{Chaudhury}}$ = 0.30 nm, considering the nanosheet as a cylinder with radius equal to the height h and length equal to the lateral side l. The same considerations done for the bipyramids are also valid for the nanosheet, and we have demonstrated that tip-sample-substrate deformations are not so relevant; moreover, consider that the adhesion terms are always overestimated.

Table 7. Uncertainty budget of the nanosheet height 'h'.

quantity X_i	estimate x_i	standard uncertainty $u(x_i)$	unit	probability distribution	sensitivity coefficient c_i	standard uncertainty $u_i(h)$ [nm]
repeatability h_m	9.3	0.1	nm	N	C_z	0.1
C_z factor	1	0.08	-	N	b_m	0.7
reference plane δ_{pl}	0	0.8	nm	R	0.58	0.5
levelling δ_{lev}	0	0.3	nm	R	0.58	0.2
tip-sample-substrate interactions δ_{int}	0.4	0.2	nm	R	0.58	0.1
mechanical drifts δ_{str}	0	0.4	nm	R	0.58	0.2
				combined standard uncertainty $u_c(h)$		0.9
				degrees of freedom ν_{eff}		190
				coverage factor k		2
				expanded uncertainty $U(h)$		1.8

Table 8. Uncertainty budget of the nanosheet lateral side 'l'.

quantity X_i	estimate x_i	standard uncertainty $u(x_i)$	unit	probability distribution	sensitivity coefficient c_i	standard uncertainty $u_i(l)$ [nm]
repeatability c_m	75	2.6	nm	N	C_X	2.6
C_X factor	1	0.02	-	N	c_m	1.3
tip dilation isotropy $\delta_{dil_{iso}}$	0	2.0	nm	N	1	2.0
tip dilation wear δ_{dil_w}	0	2.8	nm	R	0.58	1.6
			combined standard uncertainty $u_c(l)$			3.9
			degrees of freedom ν_{eff}			140
			coverage factor k			2
			expanded uncertainty $U(l)$			7.8

Table 8 reports the uncertainty budget of the nanosheets lateral dimension l, in which is considered the repeatability in the analysis of 100 nanosheets. The X-size contribution is evaluated as described for the budget in Table 6, while the tip dilation is due to (i) the tip wear δ_{dil_w}, evaluated as explained above, and (ii) the tip isotropy, evaluated through the analysis of the lateral enlargement of the dilation profile taken by the same tip on subsequent images along the X and Y scan axes. Note that the model equation is $l = C_X \cdot l_m + \delta_{dil_w} + \delta_{dil_{iso}}$.

6. Conclusions

In this work, we focused on the study of non-spherical nanoparticles using a metrological AFM. These measurements are very challenging due to both the particle and the finite tip shapes. For this reason, CSs on single NP are determined by means of geometric approaches, which consider the nominal morphological characteristics due to the conditions in which the particle have been synthesized. These methods permit to directly study peculiar shape descriptors in a robust and accurate way. The geometrical approach developed for the analysis of bipyramids CSs is based on two assumptions: (i) the presence of a square base bipyramid, due to the anatase crystal, and (ii) the isotropy of the tip shape at its apex. The nanosheet geometric analysis is based on its geometry (a truncated tetragonal bipyramidal shape squashed along the [001] axis) and on the anatase interfacial angle ϑ = (68.3 ± 0.3)°. By using this angle, it is possible to "slice" the cross-section profile into various segments, describing the nanosheet lateral dimension and the tip dilation.

These NPs with complex geometry are studied to be candidate reference materials because of the stability of the dimensions and the monomodal distribution of the CSs. In fact, measurements carried out in summertime and in the following winter in samples stored in a laboratory with controlled environment, shows a good stability of the sizes: the bipyramids CSs are b = (43.2 ± 3.4) nm and c = (58.2 ± 5.2) nm, and the nanosheets are described by the height h = (9.3 ± 1.4) nm and the lateral size l = (75 ± 26) nm. The mean

values of these NPs by mAFM measurements are well in agreement with TSEM measurements, and standard deviation are also entirely analogous.

Each reference measurand is quantitatively characterized together with its uncertainty. The intent is to estimate the different sources of systematic errors and the uncertainty associated with their corrections. For the bipyramids, combined standard uncertainty of 4% for b and 5% for c are evaluated. For the nanosheets, a combined standard uncertainty of 10% for the height h is evaluated; even if is not considered the lateral dimension l as reference because of its polydispersity, a combined standard uncertainty of 5% is also evaluated.

Please note that for the CSs calculated as top-height of a profile, *i.e.* b and h, the main uncertainty contribution is due to the definition of the reference plane, that is the mean z-height of the baseline. For c and h, instead, beyond repeatability, the dilation due to tip geometry is the predominant term in the budget.

Moreover, a quantitative characterisation of these complex shape NPs included the study of shape descriptors, which are morphological descriptors depending by CSs, and finiture descriptors depending on surface roughness. It is worth noting that these parameters make easier to quantitatively compare the same characteristic from data taken by different laboratories and/or instrumental techniques.

Through the analysis of the shape descriptors, it is possible to understand the quality of the bipyramid. The main parameter is the elongation of about 1.4 (and its inverse aspect ratio), indicating a perfect truncated shape.

The analysis of the nanosheets roughness R and texture S parameters indicates that these nanoparticles have a roughness low enough to be used as reference in nanometrology, since the surfaces area ratio Sdr is $(0.18 \pm 0.10)\%$. Furthermore, roughness amplitude parameters are studied, and besides average and Ra and Sa rms values Rq and Sq, also skewness and kurtosis are investigated. For the nanosheets, the kurtosis Sku is around three for areal parameters (normal distribution of peaks and valleys), while the profiles show a presence of broader peaks and valleys (Rku = 2.56 ± 0.69). The skewness is slightly negative ($Rsk \sim Ssk \sim$ -0.60), confirming the presence of valleys, so this parameter describes the possible presence of electronic defects or lattice vacancies on the anatase crystals.

Glossary

$\alpha_{tip-sam}$: tip-sample interaction

$\alpha_{tip-sub}$: tip-substrate interaction

$\alpha_{sam-sub}$: sample- substrate interaction

ϑ: interfacial angle of anatase TiO_2 crystals

v: Poisson ratio

~~v_i: degrees of freedom~~

v_{eff}: degrees of freedom Welch–Satterthwaite

AR: aspect ratio

B: builkiness

b: "breadth" of the bipyramid, minimum Feret

c: "length" of the bipyramid, maximum Feret

c_i: sensitivity coefficient

cmp: compactness

CD: critical dimensions

CS: critical size

e: tip enlargement

E: Young modulus

El: elongation

f: segment dependent on ϑ

GUM: Guide to the expression of Uncertainty in Measurement

h: nanosheet height

HAR: high aspect ratio

INRiM: Istituto Nazionale di Ricerca Metrologica

k: coverage factor

l: nanosheet lateral side

l_{top}: constant segment of the nanosheet

mAFM: metrological Atomic Force Microscope

NMI: National Metrology Institute

NP: nanoparticle

P: intersection of two linear regression lines fitting the top and the left/right sidewall of a nanosheet

Ra: average roughness of a profile

Rku: kurtosis of a profile

Rq: root mean square roughness

Rsk: skewness of a profile

Rz: maximum height of the roughness profile

RM: reference material

rms: root mean square

Rnd: roundness

Sa: average texture of a surface

Sku: kurtosis of a surface

Sq root mean square height within the surface

Ssk: skewness of a surface

Sz: maximum height of a surface

SEM: Scanning Electron Microscopy

Si: silicon

SI: International System of Units

PTB: Physikalisch-Technische Bundesanstalt

TEM: Transmission Electron Microscopy

TiO_2: titanium dioxide

TSEM: Transmission-mode Scanning Electron Microscopy

U: expanded uncertainty

$u_i(y)$: uncertainty contribution to the estimated quantity y

$u_c(y)$: combined standard uncertainty

Y: measurand

y: estimate of Y

x_i: contributions that affect the estimated quantity y

X_i: contributions that affect the measurand Y

X: nanosheet measured profile

VIM: International Vocabulary of Metrology

Acknowledgments

Declaration of interests

The authors declare that they have no known competing financial interests or personal relationships that could have appeared to influence the work reported in this paper.

ORCID iDs

Valter Maurino https://orcid.org/0000-0001-8456-525X

Francesco Pellegrino https://orcid.org/0000-0001-6126-0904

Gian Bartolo Picotto https://orcid.org/0000-0002-7014-0629

Luigi Ribotta https://orcid.org/0000-0001-5334-5246

References

[1] A. Mech, W. Wohlleben, A. Ghanem, V-D Hodoroaba, S. Weigel, F. Babick, R. Brüngel, C. M. Friedrich, K. Rasmussen, H Rauscher, Nano or Not Nano? A Structured Approach for Identifying Nanomaterials According to the European Commission's Definition, Small, 2020, 16, 2002228, DOI: 10.1002/smll.202002228

[2] D. Imbraguglio, A. M. Giovannozzi, A. M. Rossi, Nanometrology, Proceedings of the International School of Physics "Enrico Fermi" – Course 185 "Metrology and Physical Constants", edited by E. Bava, M. Kuhne, A. M. Rossi (IOS, Amsterdam; SIF, Bologna) 2013, DOI 10.3254/978-1-61499-326-1-193

[3]   EMPIR   Traceable   three-dimensional   nanometrology   (3D   Nano)   project, https://www.ptb.de/emrp/15sib09-project.html

[4] F. Babick, R. Boyd, A. Braun, I. Busch, H.-U. Danzebrink, L. Depero, K. Dirscherl, T. Dziomba, E. Eriksson, K. Franks, M. Gee, P.-E. Hansen, N. M. Jennett, V. Kestens, L. Koenders, M. Krumrey, J. Lausmaa, R. Leach, L. Pendrill, A. Pidduck, S. Put, G. Roebben, D. Roy, M. Stintz, R. Turan, A. Yacoot, Introductory Guide to Nanometrology, edited by P.-E. Hansen, G. Roebben, Coordination of Nanometrology in Europe project (FP7 CSA-CA 218764), 2010, ISBN: 978-0-9566809-1-4

[5] R. Herrera-Basurto, B. M. Simonet, Nanometrology, Encyclopedia of Analytical Chemistry, 2013, DOI: 10.1002/9780470027318.a9177

[6] https://www.nanoscale.ptb.de/nanoscale-standards.html, web access November 2020

[7] G. Dai, F. Zhu, M. Heidelmann, G. Fritz, T. Bayer, S. Kalt, J. Fluegge, Development and characterisation of a new line width reference material, Meas. Sci. Technol. 26 (2015) 115006, DOI: 10.1088/0957-0233/26/11/115006

[8] S. Banerjee, D. D. Dionysiou, S. C. Pillai, Self-cleaning applications of TiO_2 by photo-induced hydrophilicity and photocatalysis, *Applied Catalysis B: Environmental*, 176–177, 2015, 396-428, DOI: 10.1016/j.apcatb.2015.03.058

[9] F. Pellegrino, F. Sordello, M. Minella, C. Minero, V. Maurino, The Role of Surface Texture on the Photocatalytic H_2 Production on TiO_2, Catalysts, 2019, 9, 32, DOI: 10.3390/catal9010032

[10] L. Mino, F. Pellegrino, S. Rades, J. Radnik, Joerg; V.-D. Hodoroaba, G. Spoto, V. Maurino, G. Martra, Beyond shape engineering of TiO_2 nanoparticles: post-synthesis treatment dependence of surface hydration, hydroxylation, Lewis acidity and photocatalytic activity of TiO_2 anatase nanoparticles with dominant {001} or {101} facets, *ACS Applied Nano Materials*, 2018, 1 (9), pp 5355–5365, DOI: 10.1021/acsanm.8b01477

[11] F. Pellegrino, F. Sordello, L. Mino, C. Minero, V.-D. Hodoroaba, G. Martra, V. Maurino, Formic Acid Photoreforming for Hydrogen Production on Shape-Controlled Anatase TiO_2 Nanoparticles: Assessment of the Role of Fluorides, {101}/{001} Surfaces Ratio, and Platinization, *ACS Catal.* 2019, 9, 6692–6697, DOI: 10.1021/acscatal.9b01861

[12] U. Mansfeld, F. Pellegrino, V. Maurino, S. Marguet, F. Testard, O. Tache, V-D Hodoroaba, Towards Accurate Analysis of Particle Size Distribution for Non-Spherically Shaped Nanoparticles as Quality Control Materials, Microsc. Microanal., 25 (Suppl 2), 2019, 2328-2329, DOI: 10.1017/S1431927619012376

[13] G. B. Picotto, M. Pisani, A sample scanning system with nanometric accuracy for quantitative SPM measurements, Ultramicroscopy, 01 Jan 2001, 86(1-2), 247-254, DOI: 10.1016/s0304-3991(00)00112-1

[14] J. S. Villarrubia, Algorithms for Scanned Probe Microscope Image Simulation, Surface Reconstruction, and Tip Estimation, J. Res. Natl. Inst. Stand. Technol., 1997, 102(4):425-4544, DOI: 10.6028/jres.102.030.

[15] A. Yacoot, L. Koenders, Aspects of scanning force microscope probes and their effects on dimensional measurement, *J. Phys. D: Appl. Phys.*, 2008, 41, 103001, DOI: 10.1088/0022-3727/41/10/103001

[16] F. Tian, X. Qian, J. S. Villarrubia, Blind estimation of general tip shape in AFM imaging, *Ultramicrosopy*, 2008, 109(1):44-53, DOI: 10.1016/j.ultramic.2008.08.002

[17] E. E. Flater, G. E. Zacharakis-Jutz, B. A. Dumba, I. A. White, C. A. Clifford, Towards easy and reliable AFM tip shape determination using blind tip reconstruction, *Ultramicroscopy*, 2014, 146, 130-143, DOI: 10.1016/j.ultramic.2013.06.022

[18] H. Itoh, T. Fujimoto, S. Ichimura, Tip characterizer for atomic force microscopy, Review of Scientific Instruments, 77, 103704 (2006), DOI: 10.1063/1.2356855

[19] G. Dai, K. Hahm, H. Bosse, R. G. Dixson, Comparison of line width calibration using critical dimension atomic force microscopes between PTB and NIST, Meas. Sci. Technol., 2017, 28, 065010, DOI: 10.1088/1361-6501/aa665b

[20] N. G. Orji, H. Itoh, C. Wang, R. G. Dixson, P. S. Walecki, S. W. Schmidt, B. Irmer, Tip characterization method using multi-feature characterizer for CD-AFM, Ultramicroscopy, 2016, 162:25-34, DOI: 10.1016/j.ultramic.2015.12.003

[21] ISO 13095:2014 Surface Chemical Analysis — Atomic force microscopy — Procedure for in situ characterization of AFM probe shank profile used for nanostructure measurement, Geneva, https://www.iso.org/standard/52800.html, web access May 2021

[22] M-H Trinh, M. Odorico, L. Bellanger, M. Jacquemond, P. Parot, J-L Pellequer, Tobacco mosaic virus as an AFM tip calibrator, Journal of Molecular Recognition, 2011, 24, 503-510, DOI: 10.1002/jmr.1118

[23] G. B. Picotto, M. Vallino, L. Ribotta, Tip–sample characterization in the AFM study of a rod-shaped nanostructure, 2020, Meas. Sci. Technol., 31, 084001, DOI: 10.1088/1361-6501/ab7bc2

[24] G. Dai, F. Zhu, M. Heidelmann, G. Fritz, T. Bayer, S. Kalt, J. Fluegge, Development and characterisation of a new line width reference material, Meas. Sci. Technol. 26 (2015) 115006 (11pp), DOI :10.1088/0957-0233/26/11/115006

[25] G. Dai, L. Xu, K. Hahm, Accurate tip characterization in critical dimension atomic force microscopy, Meas. Sci. Technol. 31 (2020) 074011 (12pp), DOI:10.1088/1361-6501/ab7fd2

[26] F. Pellegrino, R. Isopescu, L. Pellutiè, F. Sordello, A. M. Rossi, E. Ortel, G. Martra, V.-D. Hodoroaba, V. Maurino, Machine learning approach for elucidating and predicting the role of synthesis parameters on the shape and size of TiO_2 nanoparticles, Scientific Reports, 2020, 10:18910, DOI: 10.1038/s41598-020-75967-w

[27] U. Diebold, The surface science of titanium dioxide, *Surface Science Reports*, 48, 5-8, 2003, DOI: 10.1016/S0167-5729(02)00100-0

[28] H. G. Yang, C. H. Sun, S. Z. Qiao, J. Zou, G. Liu, S. C. Smith, H. M. Cheng, G. Q. Lu, Anatase TiO_2 single crystals with a large percentage of reactive facets, *Nature*, 453, 638–641, 2008, DOI: 10.1038/nature06964

[29] ISO/TC 229 – Nanotechnologies, International Organization for Standardization, Geneva, 2005, https://www.iso.org/committee/381983/x/catalogue/p/1/u/0/w/0/d/0, web access May 2021

[30] H. G. Merkus, Particle Size Measurements - Fundamentals, Practice, Quality, Springer, 2009, Springer, ISBN 978-1-4020-9016-5.

[31] S. Rades, E. Ortel, V.-D. Hodoroaba, ILC on shape of bipyramidal TiO_2 NPs by TEM, Tokyo, June 2016, https://opus4.kobv.de/opus4-bam/frontdoor/index/index/docId/38900, web access December 2020

[32] ISO 4287:1997 — Geometrical Product Specifications (GPS) — Surface texture: Profile method — Terms, definitions and surface texture parameters, Geneva, https://www.iso.org/standard/10132.html, web access December 2020

[33] ISO 25178-2:2012(en) — Geometrical product specifications (GPS) — Surface texture: Areal — Part 2: Terms, definitions and surface texture parameters, Geneva, https://www.iso.org/obp/ui/#iso:std:iso:25178:-2:ed-1:v1:en, web access December 2020

[34] E. Gualtieri, N. Pugno, A. Rota, A. Spagni, E. Lepore, S. Valeri, Role of Roughness Parameters on the Tribology of Randomly Nano-Textured Silicon Surface, Journal of Nanoscience and Nanotechnology, 11, 9244–9250, 2011, DOI: 10.1166/jnn.2011.4296

[35] L. Románszki, S. Klébert, K. Héberger, Estimating Nanoscale Surface Roughness of Polyethylene Terephthalate Fibers, ACS Omega, 2020, 5, 7, 3670–3677, DOI: 10.1021/acsomega.9b04211

[36] F. Borghi, V. Vyas, A. Podestà, P. Milani, Nanoscale Roughness and Morphology Affect the IsoElectric Point of Titania Surfaces, PLoS ONE, 2013, 8,7, e68655, DOI:10.1371/journal.pone.0068655

[37] A. Borras, A. R. Gonzalez-Elipe, Wetting Properties of Polycrystalline TiO_2 Surfaces: A Scaling Approach to the Roughness Factors, Langmuir, 2010, 2010, 26(20), 15875–15882, DOI: 10.1021/la101975e

[38] R. Bellotti, G. B. Picotto, Recent advances of the metrological AFM at INRIM, Proc. SPIE 9173, Instrumentation, Metrology, and Standards for Nanomanufacturing, Optics, and Semiconductors VIII, 917304, 2014, DOI: 10.1117/12.2061954

[39] https://www.spmtips.com/afm-tip-hq-nsc14-al-bs, web access July 2020

[40] A. Delvallée, N. Feltin, S. Ducourtieux, M. Trabelsi, J. F. Hochepied, Toward an uncertainty budget for measuring nanoparticles by AFM, Metrologia, 53, 2016, 41-50, DOI: 10.1088/0026-1394/53/1/41

[41] Scanning Probe Image Processor v. 5.1.3, Image Metrology, https://www.imagemet.com/products/spip/, web access July 2020

[42] ISO 5436-2:2012 — Geometrical product specifications (GPS) — Surface texture: Profile method; Measurement standards — Part 2: Software measurement standards, Geneva, https://www.iso.org/standard/61261.html, web access January 2021

[43] ISO Guide 30:2015, Reference materials — Selected terms and definitions, International Organization for Standardization, Geneva, https://www.iso.org/standard/46209.html, web access May 2020

[44] L. Crouzier, N. Feltin, A. Delvallée, F. Pellegrino, V. Maurino, G. Cios, T. Tokarski, C. Salzmann, J. Deumer, C. Gollwitzer, V-D Hodoroaba, Correlative Analysis of the Dimensional Properties of Bipyramidal Titania

Nanoparticles by Complementing Electron Microscopy with Other Methods, Nanomaterials 2021, 11(12), 3359, DOI:10.3390/nano11123359

[45] Q. Lu, J. Wang, A. Faghihnejad, H. Zeng, Y. Liu, Understanding the molecular interactions of lipopolysaccharides duringE.coliinitial adhesion with a surface forces apparatus, Soft Matter, 2011, 7, 19, 9366-93792011, DOI: 10.1039/c1sm05554b

[46] M. Setvín, B. Daniel, V. Mansfeldova, L. Kavan, P. Scheiber, M. Fidler, M. Schmid, U. Diebold, Surface preparation of TiO_2 anatase (101): Pitfalls and how to avoid them, Surface Science, 2014, 626, 61-67, DOI: 10.1016/j.susc.2014.04.001

[47] F. Pellegrino, E. Morra, L. Mino, G. Martra, M. Chiesa, V. Maurino, Surface and Bulk Distribution of Fluorides and Ti^{3+} Species in TiO_2 Nanosheets: Implications on Charge Carrier Dynamics and Photocatalysis, The Journal of Physical Chemistry C, 2020, 124, 5, 3141-3149

[48] F. Pellegrino, personal communication Università degli Studi di Torino, 2019

[49] JCGM 100:2008, Evaluation of measurement data — Guide to the expression of uncertainty in measurement, https://www.bipm.org/en/publications/guides/gum.html

[50] EA-4/02 guide – Expression of the Uncertainty of Measuremnts in Calibration, European co-operation for Accreditation

[51] M. J. Puttock, E. G. Thwaite, Elastic compression of spheres and cylinders at point and line contact, National Standards Laboratory Technical Paper No. 25, 1969

[52] M. K. Chaudhury, T. Weaver, C. Y. Hui, E. J. Kramer, Adhesive contact of cylindrical lens and a flat sheet, Journal of Applied Physics 80, 30 (1996); DOI: 10.1063/1.362819

[53] V. Swamy, E. Holbig, L. S. Dubrovinsky, V. Prakapenka, B. C. Muddle, Mechanical properties of bulk and nanoscale TiO_2 phases, Journal of Physics and Chemistry of Solids, 2008, 2332-2335, DOI: 10.1016/j.jpcs.2008.04.018

[54] M. A. Hopcroft, W. D. Nix, T. W. Kenny, What is the Young's Modulus of Silicon?, Journal of Microelectromechanical Systems, 19, 2, 2010, DOI: 10.1109/JMEMS.2009.2039697

[55] A. Castellanos-Gomez, M. Poot, A. Amor-Amorós, G. A. Steele, H. S. J. van der Zant, N. Agraït, G. Rubio-Bollinger, Mechanical properties of freely suspended atomically thin dielectric layers of mica, Nano Research, 5, 550–557, 2012, DOI: 10.1007/s12274-012-0240-3

[56] L. Borgese, M. Gelfi, E. Bontempi, P. Goudeau, G. Geandier, D. Thiaudière, L. E. Depero, Young modulus and Poisson ratio measurements of TiO_2 thin films deposited with Atomic Layer Deposition, Surface and Coatings Technology, 206, 8–9, 2012, 2459-2463

[57] W. N. Sharpe, B. Yuan, R. Vaidyanathan, R. L. Edwards, Measurements Of Young's Modulus, Poisson's Ratio, And Tensile Strength Of Polysilicon, Proceedings of the Tenth IEEE International Workshop on Microelectromechanical Systems, Nagoya, Japan, 424-429 (1997)

[58] A. Castellanos-Gomez, M. Poot, A. Amor-Amorós, G. A. Steele, H. S.J. van der Zant, N. Agraït, G Rubio-Bollinger, Mechanical Properties of Freely Suspended Atomically Thin Dielectric Layers of Mica, Nano Res. 2012, 5(8): 550–557, DOI 10.1007/s12274-012-0240-3